

Understanding coastal impacts by nearshore wave farms using a phase-resolving wave model



Dirk P. Rijnsdorp ^{a, b, c, d, *}, Jeff E. Hansen ^{b, d, e}, Ryan J. Lowe ^{a, b, d, e}

^a Oceans Graduate School, The University of Western Australia, Australia

^b Wave Energy Research Centre, The University of Western Australia, Australia

^c Centre for Offshore Foundation Systems, The University of Western Australia, Australia

^d UWA Oceans Institute, The University of Western Australia, Australia

^e School of Earth Sciences, The University of Western Australia, Australia

ARTICLE INFO

Article history:

Received 16 July 2019

Received in revised form

21 November 2019

Accepted 29 December 2019

Available online 31 December 2019

Keywords:

Wave energy

Wave farm

Wave energy converters

Coastal impact

Non-hydrostatic

SWASH

ABSTRACT

When extracting wave energy, arrays of wave energy converters (or wave farms) may alter surrounding wave and flow fields. This paper studies the modification of hydrodynamic processes at the coastline induced by nearshore wave farms using a recently developed phase-resolving wave-flow model. Changes to nearshore hydrodynamics were assessed for various farm configurations of submerged point-absorbers positioned 1–3 km offshore that were subject to realistic sea-states. In the lee of the farms, wave heights were attenuated and onshore directed flows were generated that extended several hundred meters shoreward but did not impinge the coast. For scenarios in which the wave shadow extended to the coast, the nearshore wave height and setup were reduced resulting in longshore pressure gradients driving longshore flows that converged in the lee of the farms. Changes were largest for compact farms at smaller offshore distances, and conversely, were significantly smaller for wider spaced arrays at greater offshore distances. Based on a bulk longshore sediment transport formulation, the converging flow patterns indicate conditions favourable for the accumulation of sediment in the direct lee and divergence of sediments at locations up/down coast from the farm, suggesting a reorientation of the shoreline in response to the wave farm configurations considered.

Crown Copyright © 2020 Published by Elsevier Ltd. All rights reserved.

1. Introduction

For wave energy to become commercially viable and supply electricity grids with significant power, wave-energy-converters (WECs) will need to be arranged in arrays of tens to hundreds of devices. Wave farms of such considerable size have the potential to significantly alter the hydrodynamics in their vicinity, primarily due to the reduction of wave energy in their lee (often referred to as the wave shadow). When constructed in close proximity to the coast, the wave shadow may extend up to the shoreline, altering the nearshore wave dynamics (e.g., reducing wave heights and altering wave setup) and nearshore circulation patterns, which together may alter sediment transport pathways resulting in accretion or erosion of beaches. A detailed understanding of the potential

coastal impacts by wave farms is thus critical to provide insight into when a wave farm may have either a favourable (e.g., providing shelter from large waves) or detrimental (e.g., enhancing beach erosion) effect on a coastal region.

As no large-scale wave farms have been constructed and only a few laboratory experiments have been conducted (e.g. Refs. [25,40,47]), due to cost and difficulty to conduct at the relevant temporal and spatial scales, our understanding of the coastal impact by wave farms primarily relies on numerical modelling studies. Various modelling tools have been developed to predict the coastal impact by wave farms, which can be broadly categorised by two model classes: phase-averaged and phase-resolving models (see Ref. [14]; for a recent overview). Both model classes rely on distinctively different approaches to simulate the (nonlinear) processes that govern the wave dynamics and the wave-structure interactions.

To accurately capture the impact of wave farms, a model needs to properly account for the wave-WEC interactions that modify the incident wave field. These perturbations to the wave field by WECs

* Corresponding author. The University of Western Australia, 35 Stirling Hwy, Crawley, Western Australia, Australia.

E-mail address: dirk.rijnsdorp@uwa.edu.au (D.P. Rijnsdorp).

can be easiest understood in the context of linear waves and by employing the superposition principle (e.g., Refs. [26,41,44]). This decomposes the interactions between the WECs and a wave field into two separate problems: the interactions of incident waves with a stationary (non-moving) WEC (i.e., the diffraction problem), and the radiation of waves resulting from the WEC motions in otherwise still water (i.e., the radiation problem). The superposition of the (undisturbed) incident wave field with the scattered waves (from the diffraction problem) and radiated waves (from the radiation problem) results in a perturbed wave field that may include regions with larger or smaller waves (due to constructive or destructive interference). Such interference patterns greatly depend on individual phases and amplitudes of the scattered and radiated waves, which in turn are controlled by the geometry and motions of the device.

Due to their computational efficiency, phase-averaged models that describe the evolution of stochastic properties of the wave field with parametrized formulations (i.e., source terms) to account for various physical processes (such as wave generation by wind, dissipation due to wave breaking and wave-wave interactions [17], have primarily been used to investigate the impact of WECs on nearshore processes. In phase-averaged models, the impact of WECs on the wave field is typically parameterised by specifying a transmission coefficient that aims to extract a certain amount of wave energy (e.g., Refs. [10,23,38]). As such, this approach does not account for the complexity of the underlying wave-structure interactions that perturb the wave field through constructive or deconstructive interference between the incident, scattered and radiated waves (which requires information on the wave phase that is absent in phase-averaged models) (e.g., Ref. [15]). Given only a limited number of comparative studies with laboratory or phase-resolved models were conducted (such as [25]), we lack a detailed understanding of the limitations of phase-averaged models when predicting wave shadows and the resulting coastal impact by wave farms. Phase-averaged models have nonetheless found widespread use to predict the attenuation of the wave field in the lee of WECs (e.g., Refs. [3,9,18,24]). They have also been used in combination with process-based morphology models to study the coastal impact of wave farms (e.g., Refs. [1,8]).

More recently, phase-resolving models have been developed to accurately capture the underlying wave-structure interactions and to provide more realistic predictions of coastal impacts (e.g., Refs. [7,29,41]). Most of these efforts have relied on a coupled approach that combines a linear wave propagation model (e.g., based on the mild-slope equations) to describe the evolution of the wave field in a coastal region, with a linear wave-structure interaction solver (e.g., based on the Boundary Element Method) to account for the WEC-induced perturbations to the wave field (e.g., Refs. [13,44,45]). By including phase information this approach allows for a more realistic prediction of the attenuation of the wave field in the lee of wave farms (e.g., Ref. [43]). The resulting wave predictions have also been used in conjunction with bulk longshore sediment transport (LST) formulas (e.g., the CERC formula) to estimate the coastal response [21]. However, this approach only capture the evolution of the wave field, and predicting changes to the nearshore flow patterns would require coupling to a circulation model (i.e., driven by the radiation stress or the vortex force formulation). To the authors' knowledge, this coupling has not been attempted.

Due to the limitations of modelling WECs within phase-averaged models and the absence of more advanced phase-resolved efforts, we lack a rigorous understanding of how wave farms may impact nearshore hydrodynamics that will ultimately be essential to understand their coastal impact. This work addresses this knowledge gap by adopting an advanced phase-resolving

wave-flow model to study the coastal impact by small to moderately sized wave farms (consisting of 5–14 submerged point absorber WECs) that are located in relative close proximity to the coast (1–3 km offshore distance) for a range of farm arrangements and wave conditions at an idealised but representative coastal region.

The modelling is based on the non-hydrostatic wave-flow model SWASH [48] that accurately accounts for the relevant (nonlinear) physical processes which dominate the coastal region. As the model is based on the Reynolds-Averaged Navier-Stokes (RANS) equations, it intrinsically captures the (nonlinear) evolution of waves over variable seabeds, and the generation of wave-induced currents (e.g., longshore and rip-currents). Recent work by Ref. [29] extended SWASH to realistically capture wave-structure interactions of a submerged point absorber WEC that perturbs the wave field (including both the scattering and radiation of waves). Importantly, the modelling framework was found to be efficient enough to be applicable at the spatial and temporal scales of interest in this work ($O(1 \text{ km}^2)$ and $O(1 \text{ h})$, respectively).

The methodology is described in Section 2, including an overview of the parameter space that was considered and the details of the numerical modelling. The impact of the wave farm on the nearshore hydrodynamics is then investigated for different wave farm lay-outs (e.g., device spacing and array configurations) and a range of wave conditions (Section 3). In particular, we identified key design parameters that determine how wave farms alter nearshore hydrodynamic processes (Section 3.2). In Section 4, a first estimate of the expected coastal response is made based on predicted flow patterns as a proxy for coastal impact and based on an empirical bulk longshore sediment transport formula. Although this work is limited to submerged point absorber WECs, we discuss the implications of our findings to other WEC types. Finally, the findings of this work are summarised in Section 5.

2. Methodology

2.1. Numerical model

To capture the impacts of wave farms on a nearshore region, we employed the (phase-resolving) non-hydrostatic wave-flow model SWASH [48]. Non-hydrostatic models like SWASH are essentially a direct numerical implementation of the RANS equations. As they solve the basic flow equations, non-hydrostatic models intrinsically account for the nonlinear hydrodynamic processes that dominate coastal regions. The accuracy with which they capture such processes primarily depends on the spatial and temporal resolution. Due to efficient numerical methods [37,39], SWASH can capture the relevant processes with coarse vertical resolutions (typically a few vertical layers are sufficient), which allows for applications at the scale of a realistic coastal region (e.g., Refs. [16,19,30]).

The non-hydrostatic approach further provides a flexible platform that can be naturally extended to account for interactions between waves and floating structures (e.g., Refs. [2,20,32]). With recent work by Ref. [29] in particular, the capability of the SWASH model was successfully extended to simulate the wave-induced response of submerged WECs and the resulting perturbations to the wave field. Importantly, the extended model retained the favourable property of the non-hydrostatic approach (accurately capturing such interactions with relatively coarse vertical resolutions), thereby permitting applications at the spatial and temporal scales that are important in this work. The reader is referred to Ref. [29] for complete details of the model used here.

2.2. Parameter space

To assess the coastal impact by arrays of WECs, a range of wave farm designs and incident wave conditions were considered that were deemed likely to govern the coastal impact. Due to the large number of types of wave-energy-devices (e.g. Refs. [5,26]), the large number of choices regarding the farm design (number of devices, array lay-out and inter-device spacing) and location (water depth and offshore distance), it was impractical to consider the full range of the potential parameter space. This study therefore aims to assess the coastal impact over a targeted parameter space (illustrated in Fig. 1), over which the coastal impacts were expected to vary appreciably (i.e., from no impact to a significant impact).

We considered arrays of three-tethered submerged point absorbers (of constant dimensions) located in close proximity to the coast (1–3 km offshore). The cylindrical submerged point absorbers maintained a constant diameter of $D = 25$ m, a height of 5 m and an initial submergence depth of 3 m. To maximise power absorption by the WECs, the power-take-off (modelled as a linear spring damper) was optimised for each wave condition using a frequency domain model for the body motions based on excitation forces and hydrodynamic coefficients (added mass and radiation damping) from a semi-analytical solution to the diffraction and radiation problem (e.g., Ref. [36]).

A set of small- to moderately-sized wave farms was considered; consisting of 5, 10 and 14 devices, arranged in 2–4 staggered rows, and with a relatively small and large inter-device spacing (as illustrated in Fig. 1 and summarised in Table 1). A small spacing (here taken to be $3D$, where D is the device diameter) will be beneficial in terms of installation costs (e.g., reduced cabling and the possibility to share foundations) but may lead to significant WEC-WEC interactions that can theoretically be beneficial but practically are more likely to be detrimental for the total power

Table 1

Parameter space of the wave farm designs. Note, only two and three rows were considered for a wave farm of 5 devices.

Wave farm design parameters	Modelled values
Number of WECs N_W	5, 10, 14
Number of rows	2, 3, 4
Inter-device spacing	$3D$, $10D$
Offshore distance O_F (km)	1, 2, 3

output (e.g., Ref. [4]). A large spacing of $10D$ was chosen based on previous work by Ref. [4]; which suggested minimal WEC-WEC interactions at such spacing.

To isolate the effects of the farm design and incident wave conditions on the coastal impact, the same longshore uniform depth profile with a constant slope of 1:50 (representative for a sandy beach) and a maximum water depth of 20 m was used across all simulations. A range of idealised, but realistic, sea-states were considered that are representative for operational conditions (during which the devices are extracting energy). Sea-states were generated based on a JONSWAP-shaped spectrum with a cosine directional distribution. The simulations covered a range of significant wave heights H_s , wave periods T_p , and (one-sided) directional spreading σ_θ (Table 2).

With 18 different wave conditions for 18 different farm designs located at 3 different offshore distances, investigating all possible combinations would result in a total of 972 simulations. Such a large number of simulations was not practical given the computational requirements of the three-dimensional phase-resolving wave-flow model. To reduce the number of simulations, we therefore considered one wave condition (referred to as the baseline wave condition, highlighted in bold in Table 2) for all farm designs and offshore distances (48 scenarios). Subsequently, the sensitivity of the coastal impact to different sea-states was tested for one farm design and all offshore distances (an additional 15 scenarios). This resulted in a total of 63 different scenarios, which was feasible on supercomputing facilities.

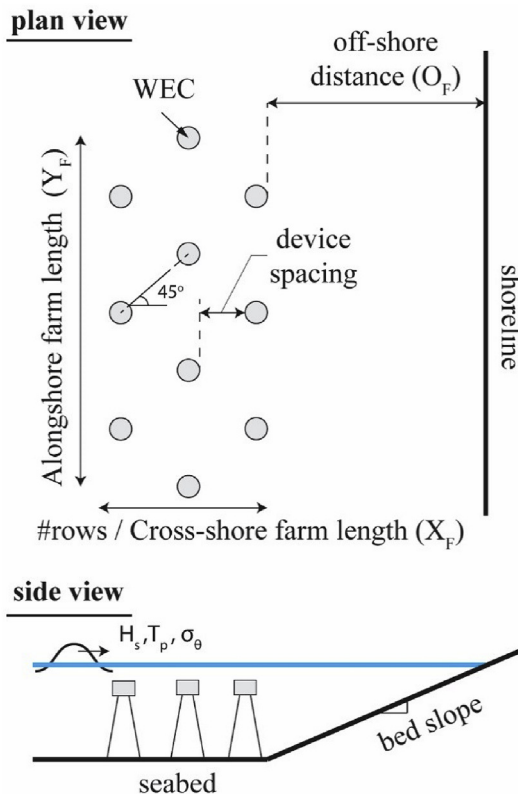


Fig. 1. Schematic diagram of the primary design parameters.

2.3. Model settings

A rectangular domain was used with horizontal dimensions depending on the size of the wave farm and its offshore distance (see Fig. 2). At the southern (offshore) side, the numerical wavemaker was positioned 500 m offshore of the first WEC. Waves were generated based on a directional JONSWAP spectra using a weakly reflective wavemaker based on linear wave theory with a second-order correction to account for bound infragravity waves (see Refs. [30,31]; for further details). Cyclic boundary conditions were used along the lateral boundaries to simulate the evolution of waves on an unbounded beach (e.g., Ref. [30]). As a result, a mirror image of the computational domain (including the wave farm) was located at both the eastern and western side of the domain. To ensure that the mirrored wave farms did not interfere with the region of interest, the WECs were located at least 1000 m away from both lateral boundaries (which was found to be sufficient, as further increases in distance had no noticeable effect on the results).

Table 2

Modelled values of the wave parameters, with bold numbers indicating the baseline wave condition.

Wave parameter	Modelled values
Significant wave height H_s (m)	1, 2 , 4
Peak period T_p (s)	8 , 10 , 15
Directional spreading σ_θ (deg)	10,2 , 31,5

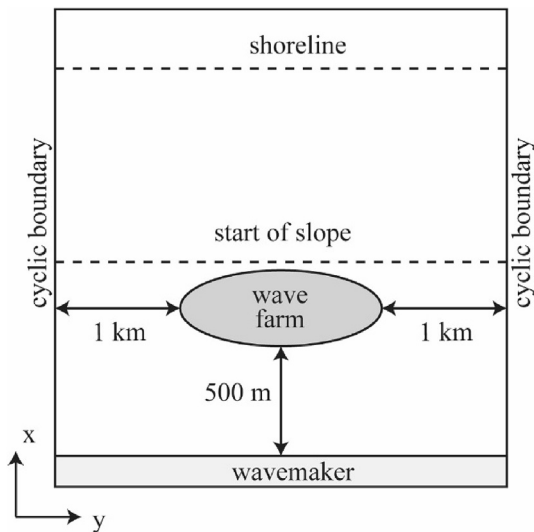


Fig. 2. Sketch of the model domain.

The accuracy of the numerical model primarily depends on the horizontal and vertical spatial resolution. For the range of scenarios considered, three vertical layers were sufficient to capture the wave dynamics (e.g. Ref. [48]), and the wave-WEC interactions (see Ref. [29] and Appendix A). To keep the computational requirements manageable while having sufficient computational grid points to capture the wave shapes, the horizontal resolution in the x-direction (Δx) was set to ensure at least 50 points per peak wave length in the offshore region, and a finer grid resolution in the surf zone (shoreward of the breakpoint) that ensured at least 30 points per peak wave length at the outer edge of the surf zone. For example, this resulted in $\Delta x = 2.5$ m in the offshore region and $\Delta x = 2$ m in the nearshore region for the baseline wave case. The longshore grid resolution, Δy , was set equal to the offshore Δx in the region covering the wave farm, and $\Delta y = 2\Delta x$ away from this to reduce the computational burden. If needed, the grid was locally refined to ensure at least 10 points per WEC diameter (in x and y-direction), which was found to be sufficient to capture the linear response of an isolated WEC (see Appendix A). In all simulations, the time step was automatically adapted to ensure that the CFL number was between 0.3 and 0.8 (with an initial time step of $\Delta t = 0.05$ s).

A constant bed friction coefficient $c_f = 0.002$, representative for a sandy coastline (e.g. Refs. [12,35]), was used throughout the numerical domain to parametrise bottom stresses. The Hydrostatic Front approximation [37] was used to initiate breaking when the temporal variation of the free-surface exceeded a threshold α . This threshold depends on the number of layers, with $\alpha = 0.6$ advised for 2 layers. We used $\alpha = 0.8$ for the three layers used in this work, which was based on a calibration study using the same laboratory data set [42] as in Ref. [37]. For each simulation, the model was run for 1 h (excluding spin-up time) to obtain quasi-steady predictions of the wave and flow field. Following the approach of [11]; a spin-up time of ~ 30 min was used in this work to ensure that the cross and longshore integrated kinetic energy, potential energy, and enstrophy (the mean square vorticity) equilibrated and fluctuated around a constant value.

2.4. Model analysis

For all scenarios, a pair of simulations (with and without a wave farm present) were run in order to quantify changes to the nearshore wave and flow field induced by the wave farm. Based on the computed instantaneous free-surface (ζ) and depth-averaged

Eulerian flow variables (u and v in the cross and longshore direction, respectively), bulk wave parameters (wave-induced setup $\eta = \bar{\zeta}$, and significant wave height $H_s = 4\sqrt{(\zeta - \eta)^2}$, where the overbars denote temporal averaging over 1 h) and flow parameters (time- and depth-averaged cross- and longshore Eulerian flow velocities, \bar{u} and \bar{v} , respectively) were output throughout the numerical domain. To gain insight in the temporal variation of the mean flow velocities (used in Section 4.1), slowly-varying depth-averaged velocities (\tilde{u} and \tilde{v} , where the tilde indicates taking a moving-average over 10 min) were output every 5 min for the last 1 h of the simulation.

For all simulations, the significant wave height at breaking (H_b), or breaking wave height, was computed by taking the maximum nearshore wave height for all cross-shore transects, which also defined the outer edge of the surf zone. To quantify changes to the longshore flow velocity, a representative depth-averaged longshore velocity V was computed for each cross-shore transect by cross-shore averaging the depth-averaged Eulerian \bar{v} over the surf zone (i.e., the region between wave breaking and the shoreline). Furthermore, depth-averaged Lagrangian flow velocities (which include Stokes drift) were computed for illustrative purposes, $\bar{u}_L = \overline{(d + \zeta)\bar{u}/(d + \zeta)}$ where d is the still water depth (e.g., Ref. [34]). In the remainder of this work, hydrodynamic parameters of the simulation without a wave farm (i.e., the reference scenario) are indicated by subscript *ref* (e.g., $H_{b,ref}$).

3. Results

In Section 3.1, we first study changes to the nearshore hydrodynamics in detail for six scenarios that help illustrate the general features of the coastal impact by nearshore wave farms. Based on these illustrative examples, general measures for the coastal impact were derived in order to compare the impact of all wave farm designs subject to the same baseline wave condition (Section 3.2). Section 3.3 subsequently presents the influence of the different sea-states on the coastal impact for a single wave farm configuration.

3.1. Changes to the nearshore hydrodynamics, six illustrative examples

For a closely spaced farm consisting of 5 devices arranged in two rows located at a distance of 1 km offshore and subject to the baseline wave condition ($H_s = 2$ m, $T_p = 10$ s, and $\sigma_\theta = 10.2^\circ$), the significant wave height H_s was reduced (by up to 30%) in the direct lee of the farm (Fig. 3a). Although the wave field “recovered” in the shoreward direction, the significant wave height at breaking H_b was still reduced by up to 0.35 m ($\approx 15\%$) in the direct lee of the farm compared to the undisturbed scenario (Fig. 3d). Changes in the wave height were strongly correlated to changes in the nearshore wave setup η along the 1 m depth contour (Fig. 3g), associated with wave dissipation through breaking and resulting cross-shore radiation stress gradients.

In the immediate lee of the WECs, onshore directed currents were predicted by the model that diverged in the longshore direction approximately 250 m shoreward of the farm (Fig. 3a). These currents were associated with gradients in wave forcing caused by the absorption of wave energy by the WECs. Near the shoreline, longshore directed currents were generated that converged in the direct lee of the farm (Fig. 3a), which were likely driven by the longshore gradients in wave setup (Fig. 3g). To illustrate the convergence of the longshore flow, Fig. 3j shows the variation along the y-axis of V , the surf zone averaged mean longshore current velocity. For this particular wave farm design, converging longshore

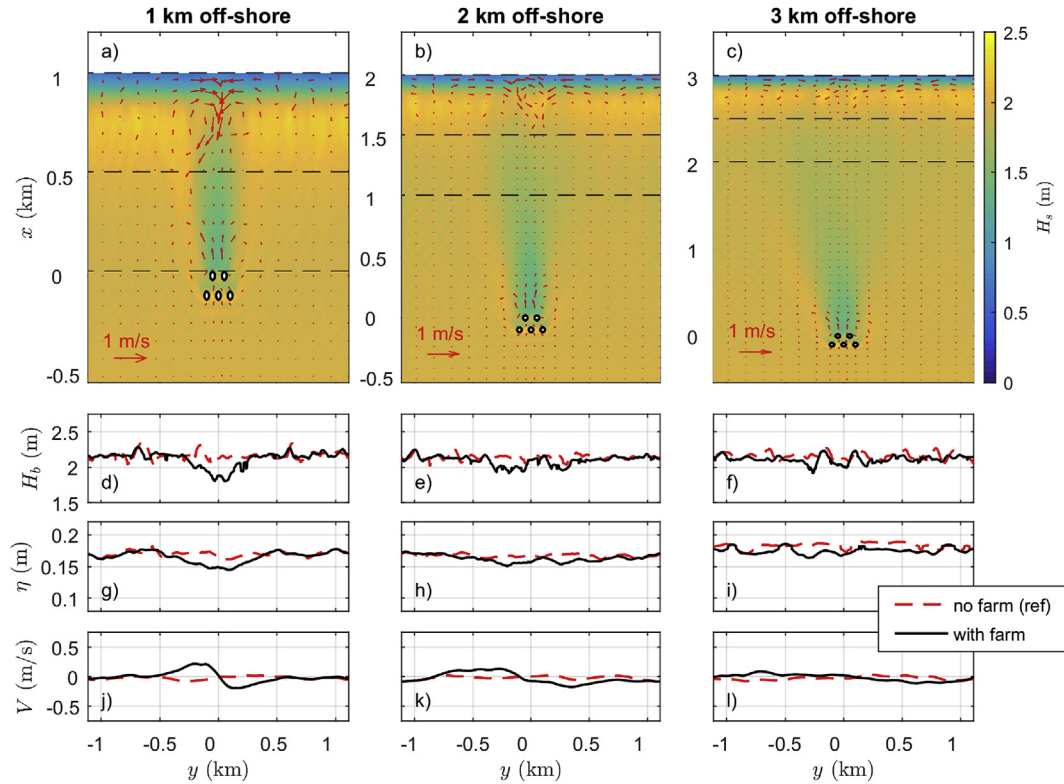


Fig. 3. Nearshore wave heights and time-averaged Lagrangian flow patterns for a small spaced array of 5 WECs arranged in two rows located 1–3 km offshore that was subject to the baseline wave condition. Panel a–c: significant wave heights H_s (colours) and Lagrangian flow field (arrows). Panel d–f: longshore variation of the significant wave height at breaking H_b , panel g–i: setup at 1 m depth contour η , and panel j–l: longshore variation of the surf zone averaged longshore current V (with positive values indicating flow in positive y -direction, left to right, and negative values indicating flow in the opposite direction, right to left). In panels a–c the dashed horizontal lines indicate the depth contours for $d = 20$ to 0 m at 10 m intervals. (For interpretation of the references to colour in this figure legend, the reader is referred to the Web version of this article.)

currents V were generated (especially compared to the reference scenario) that peaked at approximately ± 0.25 m/s at both the western and eastern side of the wave farm ($y \approx \pm 200$ m).

Results for the same wave farm located further offshore (2 and 3 km) reveal qualitatively similar results, with converging longshore flows in the nearshore (Fig. 3b–c). Due to the increased distance however, the wave field showed a stronger recovery before reaching the shoreline, leading to smaller reductions in H_b (Fig. 3e–f), smaller longshore setup gradients (Fig. 3h–i), and ultimately weaker nearshore flows (e.g., Fig. 3k–l).

For a larger wave farm consisting of 14 WECs arranged in two closely spaced rows, qualitatively similar wave and flow patterns can be observed near the shoreline (Fig. 4a–c). However, changes to the nearshore hydrodynamics were stronger for this larger farm. Even for a 3 km offshore distance, appreciable nearshore flows were generated in the nearshore region (Fig. 4c and l), associated with a significant reduction in breaking wave height (Fig. 4f) that resulted in noticeable longshore setup gradients (Fig. 4i). For the farm located 1 km from the shore, the breaking wave height showed a relatively small reduction near $y = 0$ km (Fig. 4d) due to interactions between the waves and the (strong) locally offshore directed current (Fig. 4a), illustrating the complexity of the nearshore hydrodynamic response.

Note that for all simulations the nearshore hydrodynamics (significant wave heights, and time-averaged flow patterns) showed spatial variations and asymmetric features (e.g., longshore variations in H_b and V , which even occurred for the reference scenario with no wave farm). This is not surprising given the (intrinsic) unsteady nature of the model simulations as it accounts for transient flow dynamics, such as transient rip-currents and surf zone eddies. Such variations are expected to diminish for

(significantly) longer simulation durations, which are impractical at the scales that were considered in this work.

3.2. Changes to nearshore hydrodynamics for all wave farm designs

Based on these illustrative examples, three key measures were identified that can be used to quantify the coastal impact by the wave farms: 1) the absolute change in breaking wave height $\Delta H_b = |H_b - H_{b,ref}|$, where $|\dots|$ indicates the absolute value, 2) the absolute change to the surf zone averaged mean longshore current velocity $\Delta V = |V - V_{ref}|$, and 3) the nearshore divergence of the longshore velocity $\frac{dV}{dy}$ (which is positive for converging and negative for diverging longshore currents). The above parameters all vary in space (along the y -axis), and in order to compute a single measure for each scenario, we computed both the maximum (indicated by $|\dots|_{max}$) and the longshore average in the lee of the farm (indicated by $\langle \dots \rangle$) for all three parameters, resulting in a total of six coastal impact metrics.

To understand how these metrics varied for the different wave farm designs, five parameters were identified that describe the wave farm geometry: the longshore farm length Y_F , the cross-shore farm length X_F , the offshore distance of the farm O_F , the combined surface area of all WECs $A_W (= N_W \frac{1}{4} \pi D^2)$, where N_W is the number of WECs in the wave farm), and the total surface area of the wave farm $A_F = X_F Y_F$. To study how the impact metrics varied for these parameters, we defined four non-dimensional groups based on these parameters that are expected to explain the impact of the wave farm on the nearshore hydrodynamics,

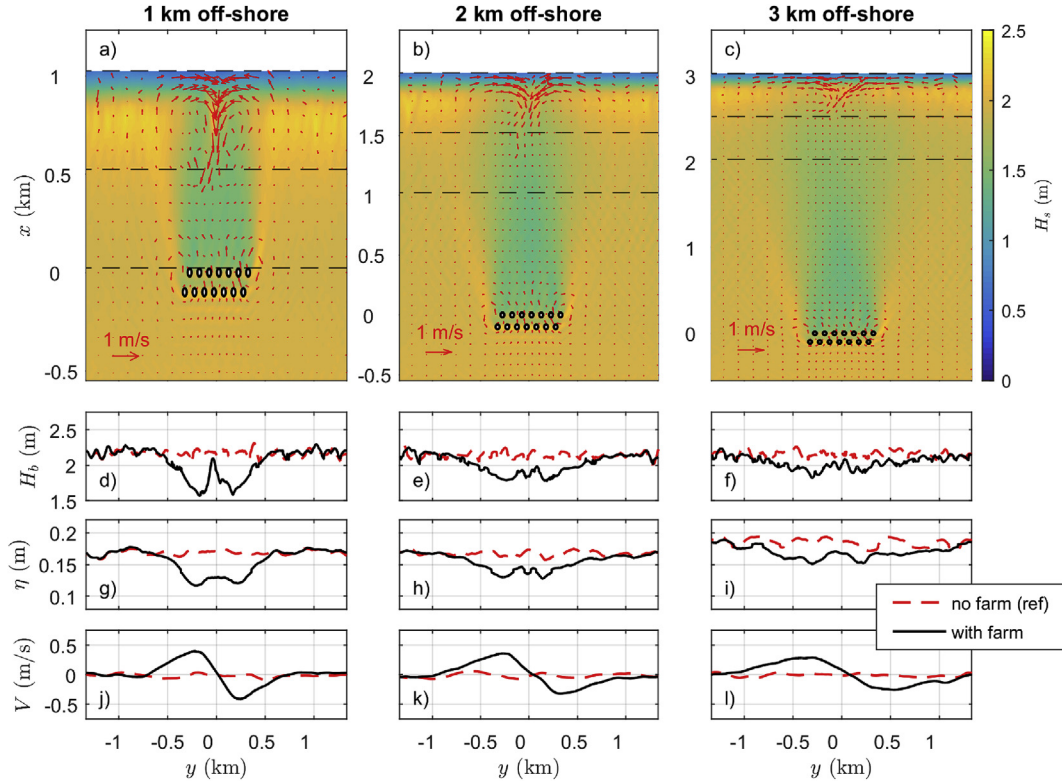


Fig. 4. Nearshore wave heights and time-averaged Lagrangian flow patterns for a small spaced array of 14 WECs arranged in two rows located 1–3 km offshore that was subject to the baseline wave condition. See the caption of Fig. 3 for further details.

$$\text{impact} = f\left(\frac{A_W}{A_F}, \frac{A_F}{L_W^2}, \frac{L_W}{O_F}, \frac{X_F}{Y_F}\right), \quad (1)$$

in which L_W is the wave length (taken here as the deep water wave length at the peak wave period $L_W = gT_p^2/(2\pi)$). In this functional relationship, $\frac{A_W}{A_F}$ is a measure of the compactness of the wave farm (differentiating between densely and widely spaced WECs), $\frac{A_F}{L_W^2}$ represents the normalised surface area of the wave farm, $\frac{O_F}{L_W}$ the normalised offshore distance, and $\frac{X_F}{Y_F}$ the aspect ratio of the wave farm. The functional form of this equation was determined for each of the six impact metrics that were defined above. The right hand side of Eq (1) was multiplied by a combination of the significant wave height (H_s) and/or peak period (T_p) of the incident sea-state to ensure that the left hand and right hand side of Eq (1) were dimensionally consistent for each impact metric. As the incident sea-state was the same for all the simulations considered in this analysis, H_s and T_p were equal for all scenarios and only served to make the equation dimensionally consistent. Note that we study the sensitivity of the coastal impact to the incident sea state separately for a single farm design in Section 3.3.

As the impact is unlikely to depend on a linear combination of these non-dimensional group in Eq. (1), we considered the following functional form of Eq. (1),

$$\text{impact} = aX\left(\frac{A_W}{A_F}\right)^b\left(\frac{A_F}{L_W^2}\right)^c\left(\frac{L_W}{O_F}\right)^d\left(\frac{X_F}{Y_F}\right)^e \quad (2)$$

in which $a - e$ are unknown empirical coefficients, and X is a combination of H_s and/or T_p to make the equation dimensionally consistent. To find the coefficients and thereby the functional form

that best describes the variability of the six impact metrics, we computed the coefficient of determination (R^2) of a linear fit to the data of each metric for a range of values (-10 to $+10$) for the coefficients ($a - e$). Subsequently, we searched for the values of the five coefficients in the functional form that provided the best fit (largest R^2) to the data of each impact metric.

Fig. 5 shows the functional form for each impact metric that led to the best least-squares fit to the simulation results. For all impact metrics, the results collapsed with $R^2 \geq 0.7$, indicating that the functional form accounts for at least 70% of the variance of the impact metrics for the considered wave farm designs. The magnitude of the six impact metrics varied significantly across the different wave farm designs, with maximum reductions in the breaking wave height varying between $\approx 0.1 - 0.75$ m (Fig. 5a) and maximum changes to the surf zone averaged mean longshore current varying between $\approx 0.1 - 0.6$ m/s (Fig. 5b). Although the magnitude of the (maximum and longshore averaged) nearshore flow velocities differed greatly over the parameter space (Fig. 5b–e), flow patterns were qualitatively similar as the longshore flows were found to converge for all simulations (as indicated by the positive $\left|\frac{dV}{dy}\right|_{\max}$ and $\left\langle\frac{dV}{dy}\right\rangle$).

The powers of the non-dimensional group in Eq. (2) (shown in the labels of Fig. 5 for each impact metric) further illustrate the relative importance of each group with respect to the coastal impact. For all metrics, the ratio of the cross-shore and longshore farm length $\frac{X_F}{Y_F}$ did not significantly alter the impact metrics, as indicated by the relatively small power ($e \leq 0.3$), and as excluding this non-dimensional group from the functional form only reduced R^2 by an average of 0.04 across all six impact metrics. This indicates that the aspect ratio of the farm did not significantly influence wave farm induced changes to the nearshore hydrodynamics. The other

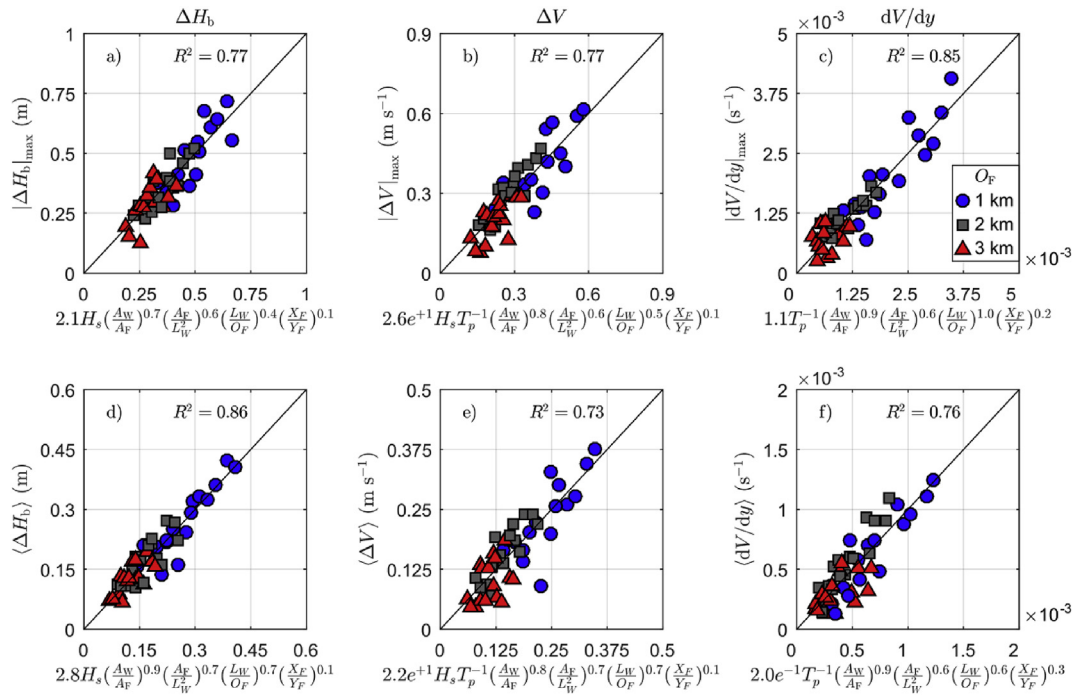


Fig. 5. The dependence of the six impact metrics on the non-dimensional groups identified in Section 3.2. Maximum (panel a–c) and longshore averaged (panel d–f) change to the nearshore breaking wave height ΔH_b (panel a and d), surf zone averaged mean longshore current ΔV (panel b and e), and longshore velocity divergence $\frac{dV}{dy}$ (panel c and f) for all wave farms subject to the baseline wave condition ($H_s = 2 \text{ m}$, $T_p = 10 \text{ s}$, $\sigma_\theta = 10.2^\circ$). The black line indicates the best fit linear relation (with the coefficient of determination R^2 shown in each panel, and the optimal functional form indicated in the label of each subpanel). The marker types and colours highlight the offshore distance: 1 km (blue circles), 2 km (grey squares), and 3 km (red triangles). (For interpretation of the references to colour in this figure legend, the reader is referred to the Web version of this article.)

three groups (representing the influence of the farm compactness, the farm area, and the offshore distance) had a comparable influence on the coastal impact as their respective powers were of similar magnitude, although the powers varied slightly across the different impact metrics. From these results, the influence of the

offshore distance O_F (as indicated by the marker colours in Fig. 5) was particularly striking, highlighting that coastal impacts were significantly larger for wave farms located closer to the coast. Overall, the results indicated that the coastal impact of nearshore wave farms (i.e., reduction in breaking wave height, and change to

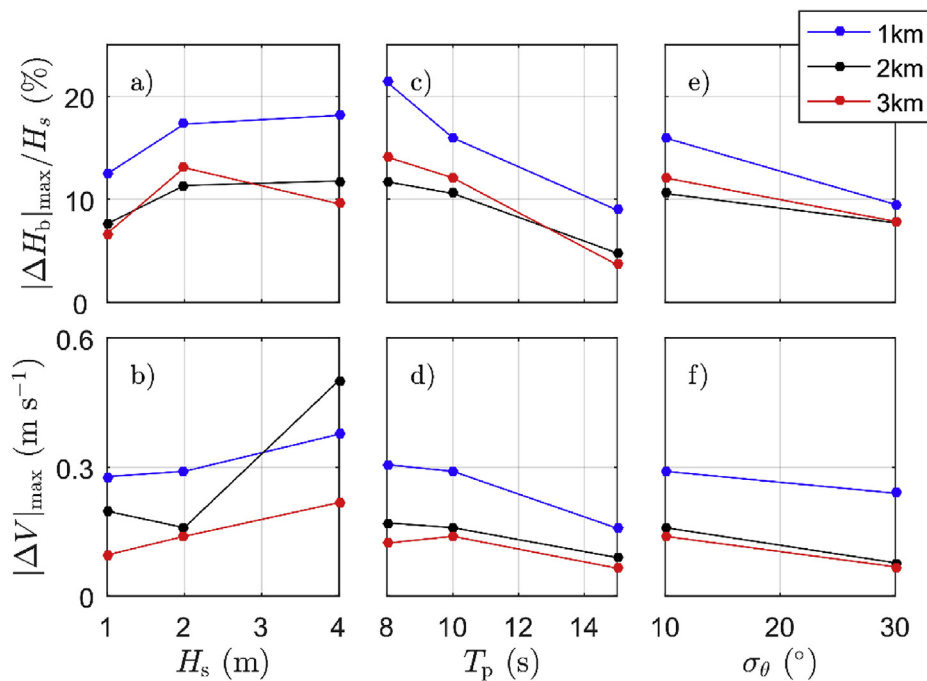


Fig. 6. Maximum change to normalised breaking wave height (1st row), and surf zone averaged mean longshore-current (2nd row) for a varying incident wave height H_s (panel a–b), peak period T_p (panel c–d), and directional spreading σ_θ (panel e–f) for a small array of 5 WECs arranged in two rows located 1 km (blue lines), 2 km (black lines) and 3 km (red lines) offshore. (For interpretation of the references to colour in this figure legend, the reader is referred to the Web version of this article.)

the nearshore longshore current) typically increased for denser farms (higher $\frac{A_w}{A_f}$), larger wave farm areas (higher $\frac{A_f}{L_w^2}$), and smaller offshore distances (higher $\frac{L_w}{O_f}$).

3.3. Sensitivity to wave conditions

To investigate how sensitive the coastal impacts by nearshore wave farms are to different wave conditions, Fig. 6 shows how $|\Delta H_b|_{max}$ (normalised by the incident H_s for illustrative purposes) and $|\Delta V|_{max}$ varied as a function of the incident significant wave height H_s (Fig. 6a–b), peak wave period T_p (Fig. 6c–d) and directional spreading σ_θ (Fig. 6e–f), for a small spaced array of 5 WECs arranged in two rows located 1–3 km offshore (the same scenarios that was considered previously in Section 3.1, Fig. 3). For increasing incident significant wave heights H_s , the reduction in the normalised breaking wave height $|\Delta H_b|_{max}$ remained relatively constant for all three offshore distances. Associated with larger absolute changes to the nearshore breaking, the maximum changes to the surf zone averaged mean longshore current $|\Delta V|_{max}$ increased for larger H_s , thus indicating that there are larger coastal impacts for more energetic incident sea states. For an increasing incident peak wave period T_p and directional spreading σ_θ , both $|\Delta H_b|_{max}$ and $|\Delta V|_{max}$ decreased, indicative of reduced coastal impacts. With larger σ_θ (increasingly short-crested sea-states), the wave field recovered more rapidly in the wave shadow, resulting in smaller changes to the nearshore hydrodynamics. For an increasing peak period (and associated peak wave length), the smaller coastal impacts were likely related to the wave-structure interactions as the size of the device relative to the wave length (amongst others) determines the significance of the perturbations to the incident wave field (becoming negligible for waves much longer than the device dimensions). Although the magnitude of the impact metrics were influenced by changes to the incident sea state, the changes to the nearshore hydrodynamics were qualitatively consistent across all wave conditions, with converging nearshore circulations for the simulations that showed distinct patterns. For some of the scenarios (in particular for short-crested sea states at $O_f > 1$ km), the nearshore circulation did not show any distinct patterns, indicative of minor to negligible coastal impacts.

4. Discussion

4.1. Implications for nearshore sediment transport

For all scenarios that showed distinct nearshore circulation patterns, longshore currents were observed to converge (although of different strength) in the lee of the wave farm (as illustrated by $\langle \frac{dV}{dy} > 0 \rangle$, Fig. 5f). For submerged nearshore structures (e.g., submerged breakwaters), Ref. [28] identified that nearshore circulation patterns can be indicative of the shoreline response, with diverging nearshore flows leading to beach erosion and converging flows leading to accretive conditions. Using the flow patterns as a proxy for the shoreline response following [27]; the occurrence of persistent converging nearshore flows in the lee of the wave farms suggests that the considered wave farms will lead to the accretion of the beach in their direct lee.

The absence of diverging currents for all considered scenarios is a major difference to the study of [27]; in which both converging and diverging currents were found in the lee of submerged structures (with their occurrence strongly depending on the structural design parameters). We hypothesise that diverging nearshore currents could be generated when the onshore flows that are

generated in the lee of the wave farm (or on top of a submerged structure) impinge the coast and subsequently diverge. The absence of any diverging nearshore flows in the results of this work is likely related to the larger offshore distance of the considered wave farms (1–3 km) compared to the relatively short offshore distance (100–400 m) of the submerged structures considered by Ref. [27]. As submerged point absorbers require sufficiently deep water for operation and installation (e.g., to avoid breaking wave impacts), it is unlikely that wave farms composed of such devices can be constructed at the shallow water depths associated with these short offshore distances (we will return to this in Section 4.2).

To further study the shoreline response and understand how its magnitude varied across the different wave farms designs, longshore sediment transport patterns were obtained from a bulk longshore sediment transport formula. Such formulas provide empirical relationships between the local hydrodynamics and longshore sediment transport, and have been used as part of coastline models to forecast shoreline changes at yearly to decadal time scales (e.g., Refs. [22,33,46]). With such an analysis, we assume that longshore transport is the dominant driver for coastal changes, assume that the (cross-shore) shape of the coastal profile is stable, and neglect the morphological feedback between the nearshore waves, flows and bathymetric changes. As such, the present study only provides an initial effort to understand the expected morphological response of the shoreline to the presence of the wave farm.

In this work, we used the bulk longshore sediment transport formula proposed by Ref. [6];

$$Q_{ls} = \frac{\varepsilon}{(\rho_s - \rho)(1 - \varphi)g w_s} FV, \quad (3)$$

in which Q_{ls} is the longshore sediment transport ($m^3 s^{-1}$), ε is a transport coefficient, ρ_s is the sediment density, ρ is the water density, φ is the sediment porosity, g is the gravitational acceleration, w_s is the sediment fall velocity, F is the linear wave energy flux ($F = Ec_g$, with wave energy E and the group velocity c_g), and V is a representative mean longshore current velocity (the surf zone averaged mean longshore current velocity). In this work, we are primarily interested in how Q_{ls} varies for different farm designs (affecting the hydrodynamic parameters) but not as a function of sediment parameters (which were taken as $\rho_s = 1500 \text{ kg m}^{-3}$, $\varphi = 0.4$, and $w_s = 0.03 \text{ m s}^{-1}$, based on typical parameter values for a sandy coast). We computed F based on the significant wave height at breaking ($E = \frac{1}{8} \rho g H_b^2$) and the group velocity assuming shallow water waves at the breakpoint. To determine the response of the shoreline to the longshore sediment transport, we computed the longshore gradient of the longshore sediment transport $\frac{dQ_{ls}}{dy}$, with positive gradients indicating accumulation of sediments (i.e., beach accretion) and negative gradients indicating erosion of sediments (i.e., beach erosion).

Fig. 7 shows the resulting longshore variation of Q_{ls} and $\frac{dQ_{ls}}{dy}$ for a total of six scenarios of two wave farm designs at three different offshore distances (the same scenarios as previously considered in Figs. 3 and 4). Associated with the longshore flow patterns, Q_{ls} peaked on either side of the farm and converged in the lee of the farm (the longshore extend of the wave farm is indicated by the shaded grey region bordered by vertical dashed lines), with Q_{ls} typically being largest for farms located closer to the shore (left panels). The converging transport patterns promote accumulation of sediment in the lee of the farm, as illustrated by positive transport gradients $\frac{dQ_{ls}}{dy}$ (green shadings in Fig. 7). The convergence of

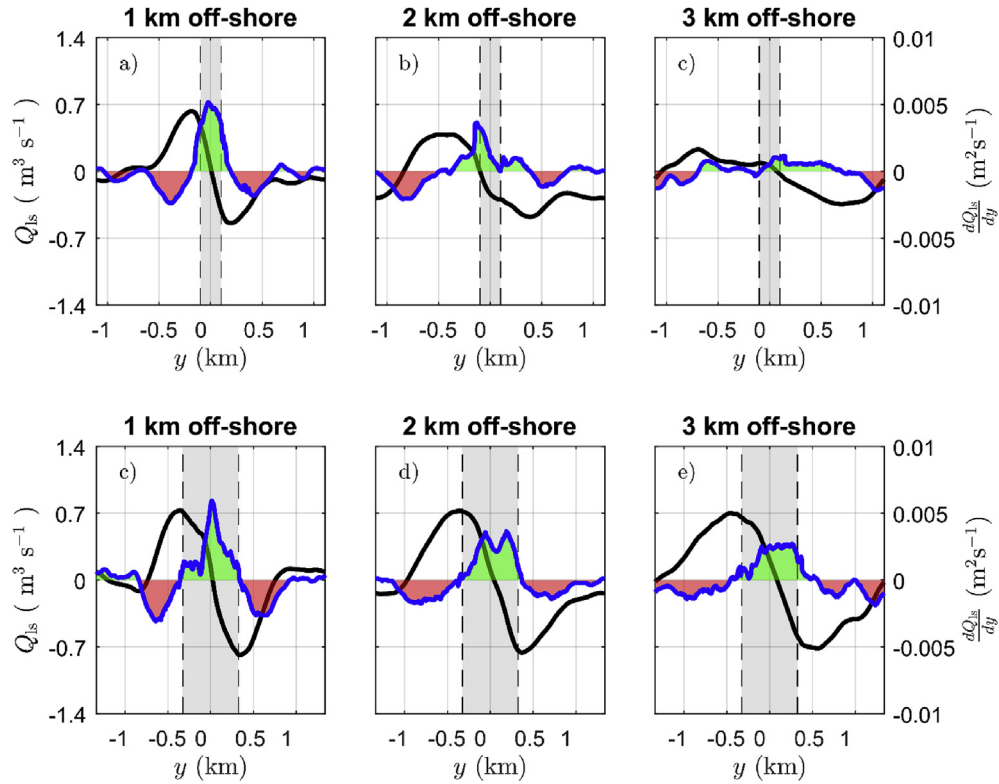


Fig. 7. Longshore sediment transport rate Q_s (black line, left axis) and longshore gradient in sediment transport rate $\frac{dQ_s}{dy}$ (blue line and coloured shades, right axis) for six different scenarios (top panels, small spaced 5 WECS arranged in three rows located 1–3 km offshore; bottom panels, small spaced 14 WECS arranged in three rows located 1–3 km offshore). The colour of the shading indicates whether sediments accumulate ($\frac{dQ_s}{dy} > 0$, green shading) or erode ($\frac{dQ_s}{dy} < 0$, red shading). The shaded grey region (bordered by vertical dashed lines) indicates the longshore extend of the wave farm (centred at $y = 0$). (For interpretation of the references to colour in this figure legend, the reader is referred to the Web version of this article.)

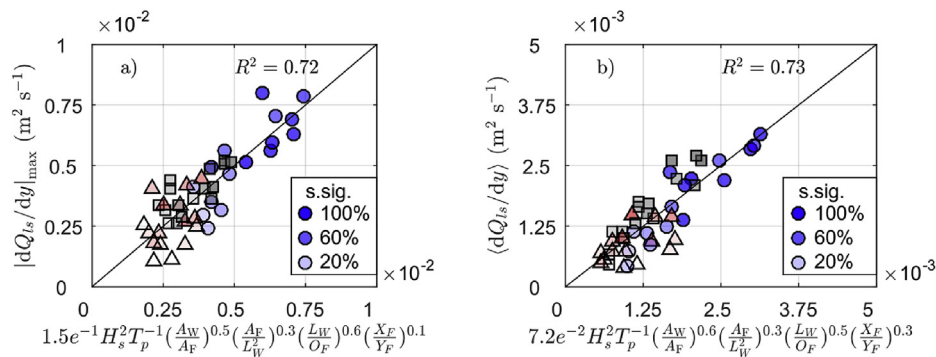


Fig. 8. Dependence of the maximum (panel a) and longshore average (panel b) longshore sediment transport gradient $\frac{dQ_s}{dy}$ on the non-dimensional groups identified in Section 3.2. The black line indicates the best fit linear relation (with the coefficient of determination R^2 shown in each panel, and the optimal functional form indicated in the label of each subpanel). The marker types and colours highlight the offshore distance: 1 km (blue circles), 2 km (grey squares), and 3 km (red triangles). The transparency of the markers indicate the percentage of cells in the lee of the farm where changes to $\frac{dQ_s}{dy}$ were statistically significant (as indicated by the legend in both panels). (For interpretation of the references to colour in this figure legend, the reader is referred to the Web version of this article.)

sediment was largest for the two farms located closer to the shore, as expected due to the larger sediment transport rates (Q_s). For all simulations, negative transport gradients occurred away of the wave farm (red shadings in Fig. 7). These results suggest that the wave farm will induce a realignment of the shoreline, with sand accreting in the lee of the wave farm but with erosion of sediments occurring further away from the wave farm.

To examine how these patterns varied across all considered wave farms subject to the same baseline wave condition, we computed the maximum and longshore average of $\frac{dQ_s}{dy}$. Fig. 8 shows the variation of the two resulting measures ($\left| \frac{dQ_s}{dy} \right|_{max}$, and $\left\langle \frac{dQ_s}{dy} \right\rangle$) as

a function of the optimal functional form (found using the same methodology as described in Section 3.2). Consistent with the changes to the nearshore hydrodynamics (Fig. 5), both metrics were typically larger for large and dense farms that are located in close proximity to the coast. For all considered scenarios, $\left\langle \frac{dQ_s}{dy} \right\rangle$ was positive, consistent with the persisting converging nearshore circulation patterns. Overall, these results suggest that an accreting initial shoreline response is most probable in the direct lee of the wave farms for the designs and baseline wave condition that were considered in this work.

To assess the statistical significance of the changes induced by a wave farm, we used a paired t -test to determine whether there was

a statistical difference between the transport gradients ($\frac{dQ_{ls}}{dy}$) of the disturbed (with wave farm) and the reference simulation (without wave farm). Note that Q_{ls} and $\frac{dQ_{ls}}{dy}$ were nonzero for the undisturbed simulation, as the nearshore wave and flow fields were quasi-unsteady (as previously discussed in Section 3.1). We used the slowly-varying Eulerian longshore velocity output (\bar{v}) of the model to compute a slowly-varying bulk sediment transport gradient $\frac{dQ_{ls}}{dy}$. This allows us to determine whether changes to $\frac{dQ_{ls}}{dy}$ in the presence of the wave farm exceeded the variability of $\frac{dQ_{ls}}{dy}$ associated with the unsteadiness of the simulations. In each longshore cell in the lee of the wave farm (indicated by the shaded grey region and vertical dashed lines in Fig. 7), we computed whether the wave farm induced change in $\frac{dQ_{ls}}{dy}$ was statistically significant, based on the rejection of the null hypothesis that the mean (temporal average) $\frac{dQ_{ls}}{dy}$ of the disturbed and reference simulation (with and without wave farm, respectively) were equal when conducting a paired t -test at a 95% confidence level. To gain a single measure for each scenario, we computed the percentage of cells in the lee of the farm where the null-hypothesis was rejected, indicating the unlikelihood that changes in $\frac{dQ_{ls}}{dy}$ were due to its intrinsic variability. In Fig. 8, the transparency of the markers indicates the percentage of cells where the null-hypothesis was rejected (e.g., 100% all cells, 0% no cells). Simulations for which $\left| \frac{dQ_{ls}}{dy} \right|_{max}$ and $\left\langle \frac{dQ_{ls}}{dy} \right\rangle$ were relatively large typically showed the largest percentage, indicating that changes to $\frac{dQ_{ls}}{dy}$ were likely related to the presence of the wave farm. On the other hand, simulations for which these two impact metrics were relatively small, the percentage was low, indicative that changes to $\frac{dQ_{ls}}{dy}$ could have been related to its intrinsic variability (and not induced by the wave farm). Overall, changes to $\frac{dQ_{ls}}{dy}$ were more often statistically significant (i.e., rejection of the null-hypothesis) for nearshore wave farms at shorter offshore distances, and especially for wave-farms with a smaller inter-device spacing (Table 3). On the other hand, for larger offshore distances, changes to $\frac{dQ_{ls}}{dy}$ were more likely to be related to its intrinsic variability rather than induced by the wave-farm, which suggests that coastal impacts by the wave farms subject to the baseline sea state became insignificant for greater offshore distances (Table 3).

4.2. Implications for other types of wave energy devices

This study considered the coastal impact by various wave farm designs for a specific WEC class (a submerged point absorber) and design (with the same dimensions used throughout this work) located in relatively close proximity to the coast (1–3 km offshore distance). Various different WEC types are currently being

Table 3
Average percentage of cells in the lee of the wave farm in which the difference between the means of $\frac{dQ_{ls}}{dy}$ of the disturbed (with wave farm) and the reference (without wave farm) simulation was statistically significant (rejection of the null-hypothesis; paired t -test, $p < 0.05$).

	Inter-device spacing		
	3D and 10D	3D	10D
WEC farms at $O_F = 1$ km	45%	60%	30%
WEC farms at $O_F = 2$ km	36%	46%	26%
WEC farms at $O_F = 3$ km	16%	20%	12%

developed (from floating point absorbers to oscillating water columns) that have different operating principles (e.g., Refs. [5,26]). Although relying on different operating principles, WECs perturb the wave field through the same fundamental wave-structure interactions: the scattering and radiation of waves that interfere with the incident wave field, which, amongst others, yield a reduction in wave energy in the lee of the WECs. Based on this premise, qualitative similar onshore directed flow patterns are expected in the direct lee of a generic wave farm (independent of the type of WEC device). We hypothesised that diverging nearshore flows, potentially leading to beach erosion, are only likely in situations where these onshore flows directly impinge on the shoreline, analogous with the occurrence of diverging currents in the lee of submerged structures [27,28]. When the onshore flows generated in close proximity of the farm diverged before reaching the coast (as was observed in this study), and in the case of a significant wave shadow in the lee of the farm that extends up to the shoreline, converging longshore current patterns (driven by longshore setup gradients due to reduced wave forcing) are more likely to dominate the nearshore region in the lee of a wave farm.

For the WEC device considered in this study, the onshore directed currents generated in the direct lee of the farm typically diverged ≈ 250 m shoreward of the farm. This indicates that wave farms composed of submerged point absorbers need to be located within a few hundred meters from the coast for diverging currents to directly impact the coast (associated with beach erosion). Given that these devices require sufficiently deep water for operation and installation, it is unlikely that such wave farms will be constructed at such short offshore distances (e.g., beach slopes of 1/20–1/100 would result in 2–10 m water depths at an offshore distance of 200 m, which is too shallow for the WEC design considered in this study). Furthermore, waves may break at such shallow water depths, which is undesirable for most WEC designs. The results of this study thus likely apply to WEC types with similar water depth restrictions. For WECs that can be constructed at the shallow water depths within a few hundred meters from the shore, further studies are required to understand their potential coastal impact.

5. Conclusions

Although various previous studies have considered the coastal impact by wave farms, we lack a detailed understanding of how wave farms induce changes to the nearshore wave and flow field. In particular, our understanding is limited as previous studies relied on the more approximate phase-averaged wave models or phase-resolving models uncoupled to circulation models. To improve our understanding of how nearshore wave farms may impact coastal processes, a recently developed (phase-resolving) non-hydrostatic wave-flow model that accurately captures the relevant hydrodynamic processes was used to systematically evaluate changes to the nearshore hydrodynamics for small to moderately sized wave farms (consisting of 5–14 submerged point absorbers) located in relative close proximity to the coast (with offshore distance of 1–3 km).

The model results showed that the wave farms considered in this study had the potential to result in significant changes to the nearshore wave and flow field. Significant wave heights at breaking and the nearshore wave-setup were reduced, resulting in the generation of appreciable nearshore currents through gradients in wave forcing. The magnitude of changes to the nearshore hydrodynamics were related to the farm design (e.g., small versus larger inter-device spacing) and the offshore distance of the farm. Changes to the nearshore hydrodynamics were largest for large dense wave farms located relatively close to the shore (1 km), and reduced for wider spaced WECs that were located at greater

offshore distances (2–3 km). The incident sea state also affected changes to the nearshore hydrodynamics, with larger incident wave heights leading to larger changes, and with greater wave periods and larger directional spreading leading to reduced changes to the nearshore hydrodynamics.

Although changes to the nearshore hydrodynamics varied in magnitude for the wave farm designs and incident wave conditions considered in the study, qualitative similar flow patterns were observed with converging nearshore currents in the direct lee of the farm. Using the flow patterns as a proxy for the shoreline response (following [27,28]) and by coupling the predicted nearshore hydrodynamics to bulk longshore sediment transport formulations, the results of this work suggested that the converging nearshore flow patterns induce an longshore convergence of sediments in the lee of the wave farm, and divergence of sediments away from the farm, resulting in a reorientation of the shoreline. Consistent with changes to the nearshore hydrodynamics, the accumulation of sediment would be largest for large dense wave farms located in closer proximity to the coast. For farms at greater offshore distances and with wider inter-device spacing, coastal impacts were reduced and for some wave farm designs became insignificant.

Although the findings of this work apply to a restricted number of nearshore wave farms consisting of a single WEC design (due to computational limitations), we hypothesised that these findings likely hold across a wider range of WEC designs due to the same underlying wave-structure interactions that alter the wave field. Based on this work, we expect that diverging nearshore flow patterns that potentially lead to beach erosion may only occur for WECs that are located within a few hundred meters from the shore. For WEC designs that can operate in the associated shallow water depths (where wave breaking may occur), further studies are required to fully understand their potential coastal impact.

Author contributions

Dirk P. Rijnsdorp: conceptualization, methodology, formal analysis, visualization, writing – original draft, writing – review & editing. **Jeff E. Hansen:** conceptualization, writing – original draft, writing – review & editing, funding acquisition. **Ryan J. Lowe:** conceptualization, writing – original draft, writing – review & editing, funding acquisition.

Declaration of competing interest

The authors declare that they have no known competing financial interests or personal relationships that could have appeared to influence the work reported in this paper.

Acknowledgements

Funding for this work was provided by the Australian Renewable Energy Agency (ARENA) as part of ARENA's Research and Development Programme in a joint project with Carnegie Clean Energy (grant number 2015RND086), and was supported by resources provided by the Pawsey Supercomputing Centre with funding from the Australian Government and the Government of Western Australia. Parts of this research were also supported by the Wave Energy Research Centre jointly funded by The University of Western Australia and the Western Australian Government (Department of Primary Industries and Regional Development, DPIRD).

Appendix B. Supplementary data

Supplementary data to this article can be found online at <https://doi.org/10.1016/j.renene.2019.12.138>.

Appendix A. Validation linear wave-induced response submerged point absorber

To ensure that the chosen grid resolution was sufficient to capture the power absorption by the wave energy devices, we compared predictions of the linear WEC response by SWASH and a linear frequency domain solution to the rigid body equations based on the hydrodynamic coefficients (added mass, and radiation damping) and wave excitation force from a semi-analytical solution to the linearized potential flow equations (see Ref. [29] for more details). Predictions by SWASH and the frequency domain model were compared for a range of linear monochromatic waves, with a height of 0.01 m and periods varying between 5 and 20 s (with 1 s increments). The power take off settings (spring and damper coefficients) were set equal to the settings in the wave farm simulations with the baseline wave condition.

The SWASH predictions captured the overall variation and typical magnitude of the normalised body motions (surge, heave, and pitch) and mean power-take-off (Fig. A1). These results confirm that the SWASH grid resolution used throughout this work was sufficient to capture the typical linear response and power absorbed by the WEC.

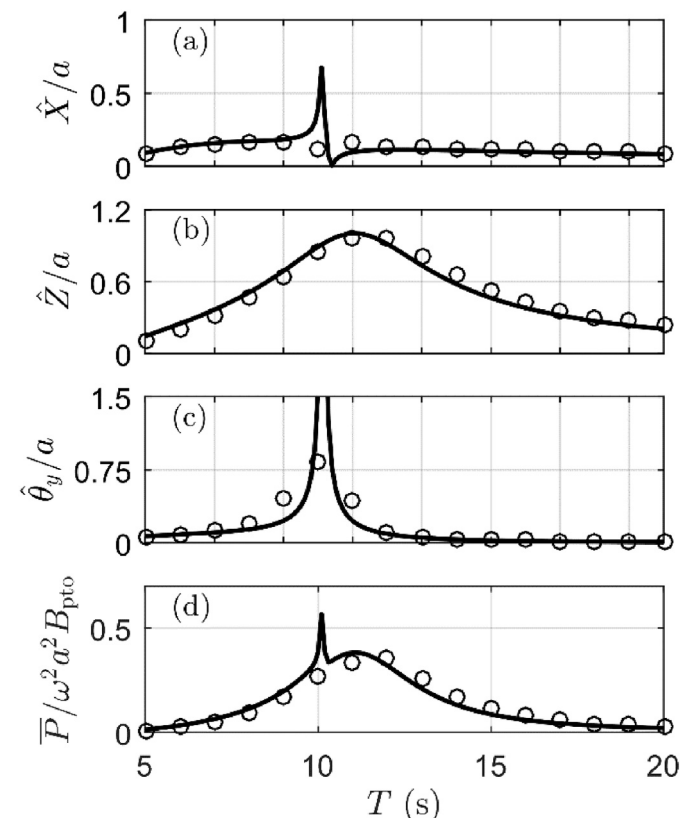


Fig. A1. Comparison between linear frequency domain model based on linear potential theory (lines) and SWASH predictions (markers) for the linear wave-induced response of a three-tethered device for an incident wave of unit amplitude. Panel a–c: response in surge \dot{X} , heave \dot{Z} , and pitch $\dot{\theta}_y$ (divided by incident wave amplitude a) versus wave period. Panel d: normalised mean power-take-off \dot{P} (where the overline indicates averaging over a wave period, ω is the radial wave frequency, and B_{pto} is the damper coefficient of the power-take off system).

References

- [1] J. Abanades, D. Greaves, G. Iglesias, Wave farm impact on the beach profile: a case study, *Coast Eng.* 86 (2014) 36–44, <https://doi.org/10.1016/j.coastaleng.2014.01.008>.
- [2] C. Ai, Y. Ma, C. Yuan, G. Dong, A 3D non-hydrostatic model for wave interactions with structures using immersed boundary method, *Comput. Fluids*

- 186 (2019) 24–37, <https://doi.org/10.1016/j.compfluid.2019.04.005>.
- [3] R. Atan, W. Finnegan, S. Nash, J. Goggins, The effect of arrays of wave energy converters on the nearshore wave climate, *Ocean Eng.* 172 (2019) 373–384, <https://doi.org/10.1016/j.oceaneng.2018.11.043>.
- [4] A. Babarit, On the park effect in arrays of oscillating wave energy converters, *Renew. Energy* 58 (2013) 68–78, <https://doi.org/10.1016/j.renene.2013.03.008>.
- [5] A. Babarit, *Ocean Wave Energy Conversion: Resource, Technologies and Performance*, Elsevier, 2017.
- [6] A. Bayram, M. Larson, H. Hanson, A new formula for the total longshore sediment transport rate, *Coast Eng.* 54 (9) (2007) 700–710, <https://doi.org/10.1016/j.coastaleng.2007.04.001>.
- [7] C. Beels, P. Troch, G. De Backer, M. Vantorre, J. De Rouck, Numerical implementation and sensitivity analysis of a wave energy converter in a time-dependent mild-slope equation model, *Coast Eng.* 57 (5) (2010) 471–492, <https://doi.org/10.1016/j.coastaleng.2009.11.003>.
- [8] R.J. Bergillos, A. López-Ruiz, E. Medina-López, A. Moñino, M. Ortega-Sánchez, The role of wave energy converter farms on coastal protection in eroding deltas, Guadalfeo, southern Spain, *J. Clean. Prod.* 171 (2018) 356–367, <https://doi.org/10.1016/j.jclepro.2017.10.018>.
- [9] R. Carballo, G. Iglesias, Wave farm impact based on realistic wave-WEC interaction, *Energy* 51 (2013) 216–229, <https://doi.org/10.1016/j.energy.2012.12.040>.
- [10] G. Chang, K. Ruehl, C.A. Jones, J. Roberts, C. Chartrand, Numerical modeling of the effects of wave energy converter characteristics on nearshore wave conditions, *Renew. Energy* 89 (2016) 636–648, <https://doi.org/10.1016/j.renene.2015.12.048>.
- [11] F. Feddersen, D.B. Clark, R.T. Guza, Modeling surf zone tracer plumes: 1. Waves, mean currents, and low-frequency eddies, *J. Geophys. Res.* 116 (C11) (2011), <https://doi.org/10.1029/2011JC007210>.
- [12] F. Feddersen, R.T. Guza, S. Elgar, T.H.C. Herbers, Alongshore momentum balances in the nearshore, *J. Geophys. Res.* 103 (C8) (1998) 15667–15676, <https://doi.org/10.1029/98JC01270>.
- [13] G. Fernández, V. Stratigaki, P. Troch, Irregular wave validation of a coupling methodology for numerical modelling of near and far field effects of wave energy converter arrays, *Energies* 12 (3) (2019) 538, <https://doi.org/10.3390/en12030538>.
- [14] M. Folley, *Numerical Modelling of Wave Energy Converters: State-Of-The-Art Techniques for Single Devices and Arrays*, Elsevier, 2016.
- [15] M. Folley, A. Babarit, B. Child, D. Forehand, L. O'Boyle, K. Silverthorne, J. Spinneken, V. Stratigaki, P. Troch, A review of numerical modelling of wave energy converter arrays, in: *Proceedings of the 31st International Conference on Ocean, Offshore and Arctic Engineering*, 2012, <https://doi.org/10.1115/OMAE2012-83807>, Rio de Janeiro, Brazil.
- [16] E.R. Gomes, R.P. Mulligan, K.L. Brodie, J.E. McNinch, Bathymetric control on the spatial distribution of wave breaking in the surf zone of a natural beach, *Coast Eng.* 116 (2016) 180–194, <https://doi.org/10.1016/j.coastaleng.2016.06.012>.
- [17] L.H. Holthuijsen, *Waves in Oceanic and Coastal Waters*, Cambridge University Press, 2007.
- [18] G. Iglesias, R. Carballo, Wave farm impact: the role of farm-to-coast distance, *Renew. Energy* 69 (2014) 375–385, <https://doi.org/10.1016/j.renene.2014.03.059>.
- [19] A.N. Lerma, R. Pedreros, A. Robinet, N. Sénéchal, Simulating wave setup and runup during storm conditions on a complex barred beach, *Coast Eng.* 123 (2017) 29–41, <https://doi.org/10.1016/j.coastaleng.2017.01.011>.
- [20] G. Ma, A.A. Farahani, J.T. Kirby, F. Shi, Modeling wave-structure interactions by an immersed boundary method in a σ -coordinate model, *Ocean Eng.* 125 (2016) 238–247, <https://doi.org/10.1016/j.oceaneng.2016.08.027>.
- [21] E. Mendoza, R. Silva, B. Zanuttigh, E. Angelelli, T. Lykke Andersen, L. Martinelli, P. Ruol, Beach response to wave energy converter farms acting as coastal defence, *Coast Eng.* 87 (2014) 97–111, <https://doi.org/10.1016/j.coastaleng.2013.10.018>.
- [22] J. Mil-Homens, R. Ranasinghe, J.S.M. van Thiel de Vries, M.J.F. Stive, Re-evaluation and improvement of three commonly used bulk longshore sediment transport formulas, *Coast Eng.* 75 (2013) 29–39, <https://doi.org/10.1016/j.coastaleng.2013.01.004>.
- [23] D.L. Millar, H.C.M. Smith, D.E. Reeve, Modelling analysis of the sensitivity of shoreline change to a wave farm, *Ocean Eng.* 34 (5–6) (2007) 884–901, <https://doi.org/10.1016/j.oceaneng.2005.12.014>.
- [24] A. O'Dea, M.C. Haller, H.T. Özkan-Haller, The impact of wave energy converter arrays on wave-induced forcing in the surf zone, *Ocean Eng.* 161 (2018) 322–336, <https://doi.org/10.1016/j.oceaneng.2018.03.077>.
- [25] H.T. Özkan-Haller, M.C. Haller, J.C. McNatt, A. Porter, P. Lenee-blum, Analyses of wave scattering and absorption produced by WEC arrays: physical/numerical experiments and model assessment, in: *Marine Renewable Energy*, 2017, <https://doi.org/10.1007/978-3-319-53536-4>.
- [26] A. Pecher, J.P. Kofoed, *Handbook of Ocean Wave Energy*, vol. 7, Springer, 2017, <https://doi.org/10.1007/978-3-319-39889-1>.
- [27] R. Ranasinghe, M. Larson, J. Savioli, Shoreline response to a single shore-parallel submerged breakwater, *Coast Eng.* 57 (11–12) (2010) 1006–1017, <https://doi.org/10.1016/j.coastaleng.2010.06.002>.
- [28] R. Ranasinghe, L.L. Turner, Shoreline response to submerged structures: a review, *Coast Eng.* 53 (1) (2006) 65–79, <https://doi.org/10.1016/j.coastaleng.2005.08.003>.
- [29] D.P. Rijnsdorp, J.E. Hansen, R.J. Lowe, Simulating the wave-induced response of a submerged wave-energy converter using a non-hydrostatic wave-flow model, *Coast Eng.* 140 (2018) 189–204, <https://doi.org/10.1016/j.coastaleng.2018.07.004>.
- [30] D.P. Rijnsdorp, G. Ruessink, M. Zijlema, Infragravity-wave dynamics in a barred coastal region, a numerical study, *J. Geophys. Res.: Oceans* 120 (6) (2015) 4068–4089, <https://doi.org/10.1002/2014JC010450>.
- [31] D.P. Rijnsdorp, P.B. Smit, M. Zijlema, Non-hydrostatic modelling of infragravity waves under laboratory conditions, *Coast Eng.* 85 (2014) 30–42, <https://doi.org/10.1016/j.coastaleng.2013.11.011>.
- [32] D.P. Rijnsdorp, M. Zijlema, Simulating waves and their interactions with a restrained ship using a non-hydrostatic wave-flow model, *Coast Eng.* 114 (2016) 119–136, <https://doi.org/10.1016/j.coastaleng.2016.04.018>.
- [33] D. Roelvink, A. Reniers, *A Guide to Modeling Coastal Morphology*, vol. 12, World Scientific, 2011.
- [34] J.S. Rogers, S.G. Monismith, F. Feddersen, C.D. Storlazzi, Hydrodynamics of spur and groove formations on a coral reef, *J. Geophys. Res.: Oceans* 118 (6) (2013) 3059–3073, <https://doi.org/10.1002/jgrc.20225>.
- [35] B.G. Ruessink, J.R. Miles, F. Feddersen, R.T. Guza, S. Elgar, Modeling the alongshore current on barred beaches, *J. Geophys. Res.: Oceans* 106 (C10) (2001) 22451–22463, <https://doi.org/10.1029/2000JC000766>.
- [36] N.Y. Sergiienko, A. Rafiee, B.S. Cazzolato, B. Ding, M. Arjomandi, Feasibility study of the three-tether axisymmetric wave energy converter, *Ocean Eng.* 150 (2018) 221–233, <https://doi.org/10.1016/j.oceaneng.2017.12.055>.
- [37] P. Smit, M. Zijlema, G. Stelling, Depth-induced wave breaking in a non-hydrostatic, near-shore wave model, *Coast Eng.* 76 (2013) 1–16, <https://doi.org/10.1016/j.coastaleng.2013.01.008>.
- [38] H.C.M. Smith, C. Pearce, D.L. Millar, Further analysis of change in nearshore wave climate due to an offshore wave farm: an enhanced case study for the Wave Hub site, *Renew. Energy* 40 (1) (2012) 51–64, <https://doi.org/10.1016/j.renene.2011.09.003>.
- [39] G. Stelling, M. Zijlema, An accurate and efficient finite-difference algorithm for non-hydrostatic free-surface flow with application to wave propagation, *Int. J. Numer. Methods Fluids* 43 (1) (2003) 1–23, <https://doi.org/10.1002/flid.595>.
- [40] V. Stratigaki, P. Troch, T. Stallard, D. Forehand, J. Kofoed, M. Folley, J. Kirkegaard, Wave basin experiments with large wave energy converter arrays to study interactions between the converters and effects on other users in the sea and the coastal area, *Energies* 7 (2) (2014) 701–734, <https://doi.org/10.3390/en7020701>.
- [41] V. Stratigaki, P. Troch, D. Forehand, A fundamental coupling methodology for modeling near-field and far-field wave effects of floating structures and wave energy devices, *Renew. Energy* 143 (2019) 1608–1627, <https://doi.org/10.1016/j.renene.2019.05.046>.
- [42] F.C.K. Ting, J.T. Kirby, Observation of undertow and turbulence in a laboratory surf zone, *Coast Eng.* 24 (1–2) (1994) 51–80, [https://doi.org/10.1016/0378-3839\(94\)90026-4](https://doi.org/10.1016/0378-3839(94)90026-4).
- [43] N. Tomez-Bozo, A. Babarit, J. Murphy, V. Stratigaki, P. Troch, T. Lewis, G. Thomas, Wake effect assessment of a flap type wave energy converter farm under realistic environmental conditions by using a numerical coupling methodology, *Coast Eng.* (2018), <https://doi.org/10.1016/j.coastaleng.2018.10.008>.
- [44] G. Verao Fernandez, P. Balitsky, V. Stratigaki, P. Troch, Coupling methodology for studying the far field effects of wave energy converter arrays over a varying bathymetry, *Energies* 11 (11) (2018) 2899, <https://doi.org/10.3390/en11112899>.
- [45] T. Verbrugge, V. Stratigaki, P. Troch, R. Rabussier, A. Kortenhuis, A comparison study of a generic coupling methodology for modeling wake effects of wave energy converter arrays, *Energies* 10 (11) (2017) 1697, <https://doi.org/10.3390/en10111697>.
- [46] S. Vitousek, P.L. Barnard, P. Limber, L. Erikson, B. Cole, A model integrating longshore and cross-shore processes for predicting long-term shoreline response to climate change, *J. Geophys. Res.: Earth Surf.* 122 (4) (2017) 782–806, <https://doi.org/10.1002/2016JF004065>.
- [47] B. Zanuttigh, E. Angelelli, Experimental investigation of floating wave energy converters for coastal protection purpose, *Coast Eng.* 80 (2013) 148–159, <https://doi.org/10.1016/j.coastaleng.2012.11.007>.
- [48] M. Zijlema, G. Stelling, P. Smit, SWASH: an operational public domain code for simulating wave fields and rapidly varied flows in coastal waters, *Coast Eng.* 58 (10) (2011) 992–1012, <https://doi.org/10.1016/j.coastaleng.2011.05.015>.